

PAPER

[View Article Online](#)
[View Journal](#) | [View Issue](#)Cite this: *Mater. Adv.*, 2022,
3, 1152Tuning crystal structure and luminescence of
 Eu^{2+} -activated $\text{LiSr}_{1-x}\text{Ba}_x\text{PO}_4$ solid solution for
white light-emitting diodes†Shuzhen Liao,^a Yao Zhang,^a Ying Li,^b Jilin Zhang, ^{*b} Zhen Chen^a and Bing Yi^{*a}

Emission spectral tuning is an important issue for phosphors. Herein, we report a Eu^{2+} -activated solid-solution $\text{LiSr}_{1-x}\text{Ba}_x\text{PO}_4$ based on a recently discovered monoclinic LiSrPO_4 , which has only one Sr^{2+} crystallographic site. Structural refinement indicates that the crystal structure can be maintained in the monoclinic phase from $\text{LiSr}_{0.995}\text{PO}_4:0.005\text{Eu}^{2+}$ ($x = 0$) to $\text{LiSr}_{0.095}\text{Ba}_{0.9}\text{PO}_4:0.005\text{Eu}^{2+}$ ($x = 0.9$). $\text{LiBa}_{0.995}\text{PO}_4:0.005\text{Eu}^{2+}$ crystallizes in a trigonal phase, with different orientations of LiO_4 and PO_4 tetrahedrons from the monoclinic one. Both Sr^{2+} and Ba^{2+} are situated in the P_6Li_6 cage that is composed of six PO_4 and six LiO_4 tetrahedrons. However, different orientations of LiO_4 and PO_4 tetrahedrons results in different coordination situations for Sr^{2+} and Ba^{2+} , which leads to two different emission bands at 420 and 470 nm for Eu^{2+} activation. It is interesting that the change of $\text{Sr}^{2+}/\text{Ba}^{2+}$ polyhedral size through solid solution does not result in a continuous shift of emission band from 420 to 470 nm, but the variation of intensity of two bands individually, which leads to the observation of both emission bands on $\text{LiSr}_{0.695}\text{Ba}_{0.3}\text{PO}_4:0.005\text{Eu}^{2+}$. The emission intensity of the phosphors at 125 °C remains 75% of the value at room temperature, suggesting good thermal stability. The performance of phosphor-converted light-emitting diodes (pc-LEDs) indicates that phosphors can be used for near-UV chip-based white pc-LEDs.

Received 13th October 2021,
Accepted 21st November 2021

DOI: 10.1039/d1ma00950h

rsc.li/materials-advances

1. Introduction

Phosphor-converted white light-emitting diodes (w-LEDs) have been widely used as solid-state lighting for illumination and backlight for display.^{1,2} The properties of phosphors are crucial for the performance of LEDs, such as luminance efficacy, thermal stability, correlated color temperature (CCT), color-rendering index (CRI), and color gamut.^{3,4} Generally, LED with high CRI value and suitable CCT are needed for illumination. Phosphors with wide emission bands are beneficial to improve CRI value and adjust the CCT value for w-LEDs. Activators with parity-allowed transition are beneficial to improve the emission efficiency of phosphors, which in turn improve the luminance efficacy of w-LEDs. Eu^{2+} and Ce^{3+} ions are such kinds of activators with allowed 5d–4f transition and broad-band

emission, which are usually utilized as activators for phosphors applied in w-LEDs.^{2,4–6}

The 5d orbitals of Eu^{2+} and Ce^{3+} ions are greatly influenced by the coordination environment. The energy difference between the lowest 5d excited level and the 4f ground level is adjustable, which in turn results in phosphors that can be excited efficiently by near-UV or blue light and exhibit color-tunable emission. Therefore, a large number of Eu^{2+} - or Ce^{3+} -activated phosphors with tunable emission color have been reported on the basis of different crystal structures.^{7–17} The modification of crystal structures through the solid solution is an efficient way to adjust the luminescent properties of Eu^{2+} - or Ce^{3+} -activated phosphors, which contains cationic replacement, (partial) anionic replacement, both cationic and anion group replacement, *etc.*⁶ These types of modification usually result in a continuous shift of the emission band, due to continuous variation of coordination polyhedron. There are other types of tuning emission colors for Eu^{2+} - or Ce^{3+} -activated phosphors, which exhibit discrete variation of emission wavelength, *i.e.* crystal-site engineering approach and nano-segregation (or mixing of phases in the nano-domain region).^{18–20}

LiSrPO_4 that can crystallize in a hexagonal (h) phase (PDF#14-0202), a monoclinic phase (PDF#53-1238), and a new

^a Hunan Provincial Key Laboratory of Environmental Catalysis and Waste Recycling, College of Materials and Chemical Engineering, Hunan Institute of Engineering, Xiangtan 411104, P. R. China. E-mail: bingyi2004@126.com

^b Key Laboratory of Light Energy Conversion Materials of Hunan Province College, Hunan Normal University, Changsha 410081, P. R. China. E-mail: chemzhangjl@hunnu.edu.cn

† Electronic supplementary information (ESI) available: Rietveld refinement, cell and atomic parameters, Sr/Ba/Eu–O distances, PL, XRD, spectra for QE, CIE versus current. See DOI: 10.1039/d1ma00950h

hexagonal phase (ICSD#258641) has been reported. Eu^{2+} -Activated phosphors with related structures were reported.^{21–23} Recently, we discovered a new monoclinic (m-) LiSrPO_4 with a higher symmetry than the old one.²⁴ A different Eu^{2+} -related luminescence was also observed. The crystal structure of the new m- LiSrPO_4 was refined based on the crystal structure of m- LiBaPO_4 reported by Kim *et al.*²⁵ The difference between crystal structures of new m- LiSrPO_4 and h- LiSrPO_4 is caused by the different orientations of LiO_4 and PO_4 tetrahedrons.²⁴ The crystal structure of LiBaPO_4 underwent monoclinic (m) \rightarrow trigonal (t) \rightarrow hexagonal (h) \rightarrow orthorhombic phase transitions upon heating from 298 to 1373 K, where the m \rightarrow t \rightarrow h transitions are displacive by the movement of polyhedrons without breaking chemical bonds.²⁵ Previous works on Eu^{2+} -activated LiBaPO_4 are all based on the hexagonal phase.^{26–30}

Since both LiSrPO_4 and LiBaPO_4 can crystallize in a monoclinic phase, a solid solution between them is expected to be obtained, which would influence the luminescence of Eu^{2+} -activation. To the best of our knowledge, this is the first time to report on the evolution of Eu^{2+} -related emission on monoclinic $\text{Li}(\text{Sr},\text{Ba})\text{PO}_4$ solid solution. In the present work, solid solution within monoclinic phase can be realized from $\text{LiSr}_{0.995}\text{PO}_4$ (PO_4):0.005 Eu^{2+} to $\text{LiSr}_{0.095}\text{Ba}_{0.9}(\text{PO}_4)$:0.005 Eu^{2+} . While trigonal phase forms for the end compound $\text{LiBa}_{0.995}(\text{PO}_4)$:0.005 Eu^{2+} without Sr^{2+} . Although there is only one crystallographic site for Eu^{2+} in these hosts, no continuous spectral shift is observed but a variation of two distinct emission bands upon increasing the Ba^{2+} content. The structure and luminescence of phosphors are studied in detail. Nanosegregation is proposed to explain the existence and intensity variation of the two emission bands.

2. Experimental

2.1. Materials and synthesis

$\text{LiSr}_{0.995-x}\text{Ba}_x\text{PO}_4$:0.005 Eu^{2+} phosphors were synthesized by using a conventional high-temperature solid-state reaction. Stoichiometric amounts of the raw materials SrCO_3 (A.R.), BaCO_3 (A.R.), Li_2CO_3 (A.R.), $\text{NH}_4\text{H}_2\text{PO}_4$ (A.R.), and Eu_2O_3 (99.99%) were thoroughly mixed in an agate mortar. The well-mixed raw materials were sintered at 1000–1300 °C for 4 hours in a reductive atmosphere (a mixture containing 5% H_2 and 95% N_2 in volume percent). The synthetic process is similar to the previous work.²⁴

2.2. Measurements and characterization

X-Ray powder diffraction (XRD) patterns were measured using a Rigaku Ultima IV diffractometer (Cu K α radiation (40 kV, 40 mA)). The XRD data for Rietveld refinements were collected under a slow scan speed in the range of 10°–120° by using a PANalytical X'pert Pro diffractometer equipped with a Cu K α radiation (40 kV, 40 mA). The refinements were achieved on a GSAS program.³¹ The photoluminescence excitation (PLE), emission (PL) spectra, and temperature-dependent PL spectra were measured on a Hitachi F-4500 spectrophotometer with a TAP-02 temperature controller (Orient KOJI). The absolute quantum efficiency (QE), decay curves were measured using

an Edinburgh FLS980 fluorescence spectrometer equipped with a 450 W Xe lamp, a 320 nm-pulsed laser, and an integrating sphere. The pc-LEDs were fabricated based on a 1 watt 365 nm chip. The electroluminescent (EL) spectra of the pc-LEDs were collected on a highly accurate array spectrometer (HSP6000, HOPOO).

3. Results and discussion

XRD patterns of $\text{LiSr}_{0.995-x}\text{Ba}_x\text{PO}_4$:0.005 Eu^{2+} ($x = 0$ –0.995) synthesized at 1200 °C are shown in Fig. 1. $\text{LiSr}_{0.995}\text{PO}_4$:0.005 Eu^{2+} ($x = 0$) contains the main phase that crystallizes in a new monoclinic (m-) phase as reported before,²⁴ and an impurity phase that can be indexed to m- LiSrPO_4 phase (PDF#53-1238) with a lower symmetry than the main phase. It should be noted that pure monoclinic $\text{LiSr}_{0.995}\text{PO}_4$:0.005 Eu^{2+} can be achieved under sintering in 1000 and 1100 °C. The diffraction peaks exhibit an obvious shift to the small angle side with the increase of Ba content (x). The impurity phase disappears with the introduction of Ba. The magnified diffraction peaks at around $2\theta = 30^\circ$ (Fig. 1b) show not only the shift of peaks but also the tendency of getting closer and finally becoming a single peak for $x = 0.995$ without Sr atoms. This phenomenon suggests the variation of cell parameters and interplanar spacing and the change of crystal structure at $x = 0.995$. Kim *et al.* reported that a slowly-cooled (-5 K h^{-1}) sample crystallized in a monoclinic LiBaPO_4 , while the quenched sample is trigonal (t)- LiBaPO_4 .²⁵ Our sample was furnace cooled, which had a much higher speed than 5 K h^{-1} . Therefore, t- $\text{LiBa}_{0.995}\text{PO}_4$:0.005 Eu^{2+} was reasonable. On the other hand, the t- LiSrPO_4 phase is not reported till now. The existence of Sr^{2+} may have great influence on the phase, therefore, all $\text{LiSr}_{0.995-x}\text{Ba}_x\text{PO}_4$:0.005 Eu^{2+} ($x = 0.1$ –0.9) samples synthesized at 1200 °C have the same phase as monoclinic $\text{LiSr}_{0.995}\text{PO}_4$:0.005 Eu^{2+} .

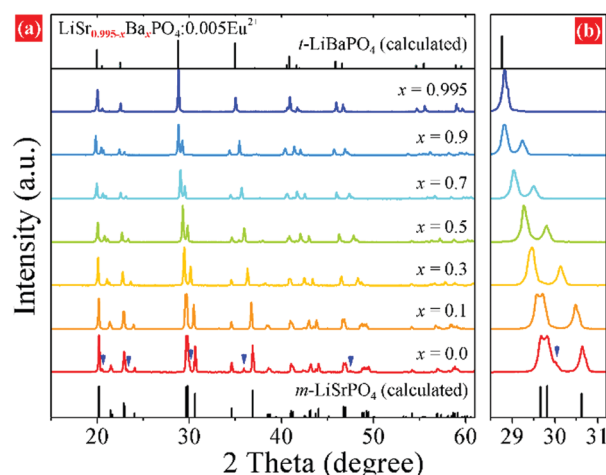


Fig. 1 (a) XRD patterns of $\text{LiSr}_{0.995-x}\text{Ba}_x\text{PO}_4$:0.005 Eu^{2+} synthesized at 1200 °C with different Ba^{2+} concentrations (x), (b) magnified XRD patterns in the 28°–31° range. Peaks assigned by arrows: impurity m- LiSrPO_4 phase (PDF#53-1238).



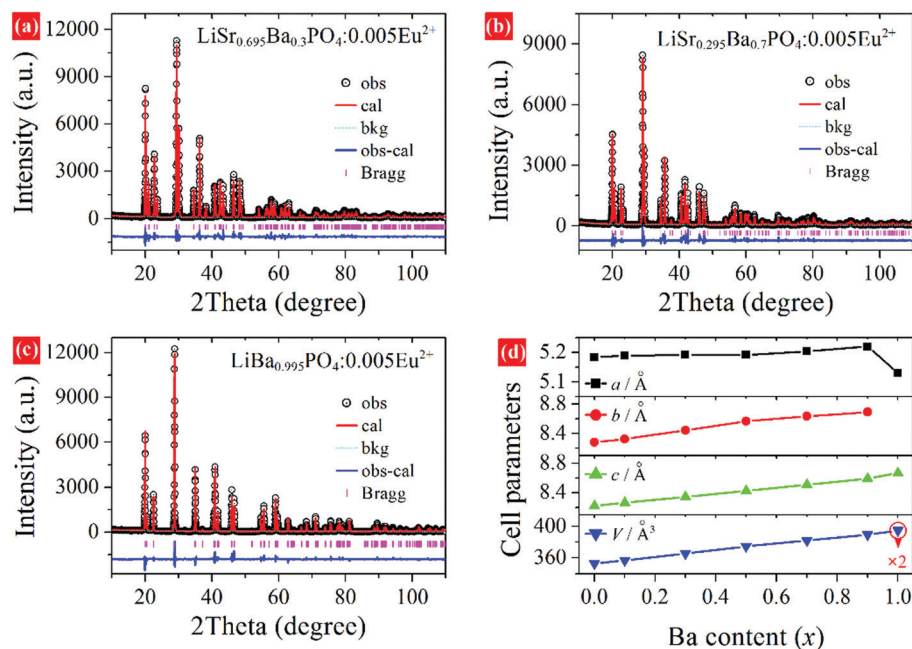


Fig. 2 Rietveld refinement of $\text{LiSr}_{0.995-x}\text{Ba}_x\text{PO}_4:0.005\text{Eu}^{2+}$ synthesized at 1200°C . (a) $x = 0.3$, (b) $x = 0.7$, (c) $x = 0.995$, (d) cell parameters versus Ba content.

Rietveld refinements were conducted to further study the variation of crystal structure in detail. The crystal data of monoclinic LiBaPO_4 reported by Kim *et al.* were used as a starting model for refinement of samples with x equaling 0–0.9.²⁵ While the refinement for $x = 0.995$ was based on the crystal structure of trigonal (*t*)- LiBaPO_4 .²⁵ Fig. 2a–c illustrate refinement results of representative samples, namely $x = 0.3$, 0.7, and 0.995 that were obtained at 1200°C . The refinement result for $x = 0$ can be found in our previous work,²⁴ and the results of others are shown in the ESI† as Fig. S1. The calculated values match well with the observed data. Fig. 2d shows the cell parameters versus Ba content (x). The cell lengths and cell volume tend to increase with Ba content. It should be noted that sample $x = 0.995$ crystallizes in a different phase compared to others, and has a half number of chemical formulas in a unit cell than others. Therefore, the two times of cell volume for $x = 0.995$ is larger than the volume of others. Detailed refinement results and crystallographic data are listed in Tables S1–S8 in the ESI.† Fig. 3 illustrates the crystal structures of representative samples viewed along the c axis. Three PO_4 and three LiO_4 tetrahedrons connect alternately and form a six-member ring. Two parallel rings are also connected by sharing three oxygen atoms, which form a P_6Li_6 cage. A Sr, Ba, or Eu atom is situated at the center of the cage. Fig. 3 shows that the degree of dislocation between the two parallel six-member rings decreases upon increasing the Ba content. Fig. 4 exhibits the difference in the positions of tetrahedrons. Samples with $x = 0$ and 0.1 have similar relative positions of PO_4 and LiO_4 , while those with $x = 0.3$ –0.995 have similar relative positions. The difference in the relative positions of PO_4 and LiO_4 tetrahedrons will result in the variation of coordination polyhedrons for Sr, Ba, and Eu. Table S9 (ESI†) lists Sr/Ba/Eu–O

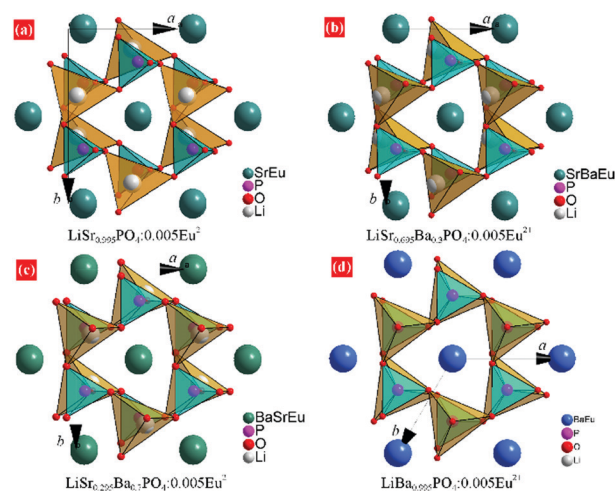


Fig. 3 Crystal structure of (a) *m*- $\text{LiSr}_{0.995}\text{PO}_4:0.005\text{Eu}^{2+}$, (b) *m*- $\text{LiSr}_{0.695}\text{Ba}_{0.3}\text{PO}_4:0.005\text{Eu}^{2+}$, (c) *m*- $\text{LiSr}_{0.295}\text{Ba}_{0.7}\text{PO}_4:0.005\text{Eu}^{2+}$, and (d) *t*- $\text{LiBa}_{0.995}\text{PO}_4:0.005\text{Eu}^{2+}$ from the refinement results.

and P–O distances obtained from refinement. The average distance of the nine-coordinated polyhedrons tends to increase with Ba content, which is in accordance with the cell volume. However, it should be noted that there is an abnormally long distance for Sr-rich samples as pointed out in Fig. 4, which is due to the relatively smaller cationic size of the P_6Li_6 cage.

The relative energy of 5d levels of Eu^{2+} depends on the coordination environment. Therefore, PLE and PL spectra are expected to be tunable by changing the x value in $\text{LiSr}_{0.995-x}\text{Ba}_x\text{PO}_4:0.005\text{Eu}^{2+}$. Fig. 5a and b show PLE and PL



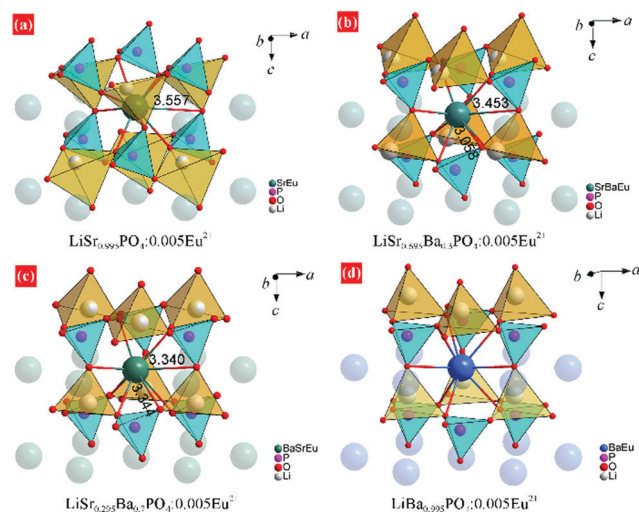


Fig. 4 Comparison of MO_9 , PO_4 , and LiO_4 polyhedrons in the crystal structures. (a) $\text{m-LiSr}_{0.995}\text{Ba}_{0.005}\text{Eu}^{2+}$, (b) $\text{m-LiSr}_{0.695}\text{Ba}_{0.305}\text{Eu}^{2+}$, (c) $\text{m-LiSr}_{0.295}\text{Ba}_{0.705}\text{Eu}^{2+}$, and (d) $\text{t-LiBa}_{0.995}\text{Eu}^{2+}$ from the refinement results.

spectra of $\text{LiSr}_{0.995-x}\text{Ba}_x\text{PO}_4:0.005\text{Eu}^{2+}$ synthesized at 1200°C . The PLE spectra of all the phosphors cover the 250–420 nm region with a maximum at around 365 nm, which indicates that all of the phosphors can be excited by near UV light. The profiles of PLE spectra for $x = 0$ and 0.1 are different from those for $x = 0.3$ – 0.995 , which relate to the difference in coordination environment for Eu^{2+} . Under excitation at 365 nm, phosphors with $x = 0$ and 0.1 exhibit a PL band at 420 nm, while those with $x = 0.5$ – 0.995 have an asymmetric PL

band at 470 nm. Phosphor with $x = 0.3$ possesses both PL bands at 420 and 470 nm. Fig. 5c shows the PL intensity of the two bands *versus* Ba content (x), which shows a rapid decrease for the 420 nm band from $x = 0$ to 0.3 and a slight increase of the 470 nm band from $x = 0.3$ to 0.995 . Fig. S2 and S3 (ESI[†]) show PL spectra and XRD patterns of $\text{LiSr}_{0.995-x}\text{Ba}_x\text{PO}_4:0.005\text{Eu}^{2+}$ synthesized at 1000 – 1300°C , respectively. Upon changing the Ba content, similar variations in PL bands and XRD peaks compared to those obtained at 1200°C were observed. The different PL profile for $\text{LiSr}_{0.995}\text{PO}_4:0.005\text{Eu}^{2+}$ ($x = 0$) obtained at 1300°C is due to the formation of the different crystal structure (m-LiSrPO_4 , PDF#53-1238), which has been discussed in our previous work.²⁴

Generally, there are two types of variation for the PL band of $\text{Eu}^{2+}/\text{Ce}^{3+}$ -activated solid solutions, where the cations occupied by an activator(s) change. The first one is a continuous shift of the PL band if the solid solution leads to the variation of a same crystallographic site occupied by Eu^{2+} or Ce^{3+} , *e.g.* $\text{Ba}_{2-x}\text{Sr}_x\text{SiO}_4:\text{Ce}^{3+}$,¹³ $\text{Sr}_{1-x}\text{Ba}_x\text{Si}_2\text{O}_7:\text{Eu}^{2+}$ ($x = 0$ – 0.75),³² $\text{Ca}_{1-x}\text{Sr}_x\text{Hf}_4(\text{PO}_4)_6:\text{Eu}^{2+}$,³³ *etc.* The second one is a discontinuous shift of the PL band if the solid solution leads to the variation of occupancy for Eu^{2+} or Ce^{3+} on more than one crystallographic sites, *e.g.* $\text{Li}_4\text{Sr}_{1+x}\text{Ca}_{1-x}(\text{SiO}_4)_2:\text{Ce}^{3+}$,¹⁸ $\text{CsKNa}_{2-y}\text{Li}_y(\text{Li}_3\text{SiO}_4)_4:\text{Eu}^{2+}$ ($y = 0$ – 1),³⁴ *etc.* It is interesting that no continuous shift of PL band is observed in $\text{LiSr}_{0.995-x}\text{Ba}_x\text{PO}_4:0.005\text{Eu}^{2+}$ series by changing the Ba/Sr ratio, where there is only one Ba/Sr crystallographic site as indicated by the refinement result. It is speculated that environments of SrO_9 and BaO_9 in $\text{LiSr}_{0.995-x}\text{Ba}_x\text{PO}_4:0.005\text{Eu}^{2+}$ ($x = 0.1$ – 0.9) are similar to those in $\text{LiSr}_{0.995}\text{PO}_4:0.005\text{Eu}^{2+}$ ($x = 0$) and $\text{LiBa}_{0.995}\text{PO}_4:0.005\text{Eu}^{2+}$ ($x = 0.995$), respectively, based on the variation of PL bands

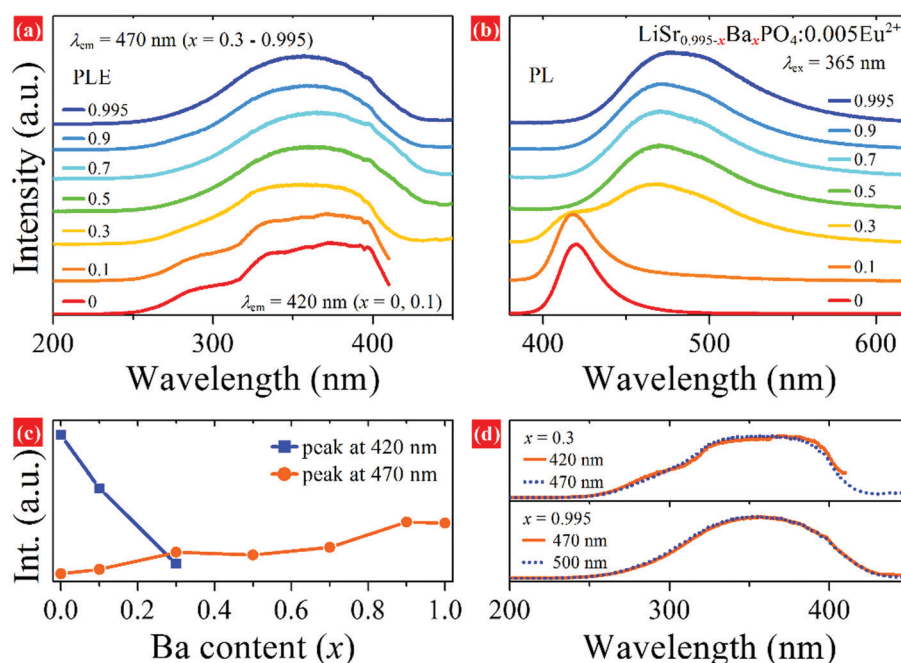


Fig. 5 PLE and PL spectra of $\text{LiSr}_{0.995-x}\text{Ba}_x\text{PO}_4:0.005\text{Eu}^{2+}$ synthesized at 1200°C . (a) PLE monitored at 420 or 470 nm, (b) PL excited at 365 nm, (c) PL intensity *versus* Ba content, (d) normalized PLE spectra monitored at two different wavelengths for $x = 0.3$ and 0.995 .

and relative PL intensities, although refinement suggests only one Ba/Sr crystallographic site. SrO_9 is dominant in samples with $x = 0$ and 0.1, which results in a 420 nm PL band after Eu^{2+} substitution. While Eu^{2+} tends to occupy the BaO_9 site for samples with $x = 0.5$ –0.995, which results in a 470 nm PL band. Eu^{2+} ions situate on both SrO_9 and BaO_9 in the sample with $x = 0.3$; therefore, two PL bands are observed. This phenomenon is similar to that in Eu^{2+} -doped $(\text{CaMg})_x(\text{NaSc})_{1-x}\text{Si}_2\text{O}_6$ solid solution, where nano-segregation occurred and allowed predictive control of the relative PL intensity of the two bands with the same profile and wavelength center to the end compounds.¹⁹ Therefore, the variation of PL spectra indicates that nano-segregation also happens in the $\text{LiSr}_{0.995-x}\text{Ba}_x\text{PO}_4:0.005\text{Eu}^{2+}$ solid solution.

The relationship between emission peak and site coordination environment can be discussed by comparing the crystal field strength (calculation of crystal field splitting), centroid shift of 5d levels for Eu^{2+} , and Stokes shift for Eu^{2+} on Sr^{2+} and Ba^{2+} sites. The average $\text{Sr}^{2+}/\text{Ba}^{2+}/\text{Eu}^{2+}$ –O distances (R_{av}) are 2.751 and 2.899 Å in $\text{LiSr}_{0.995}\text{PO}_4:0.005\text{Eu}^{2+}$ and $\text{LiBa}_{0.995}\text{PO}_4:0.005\text{Eu}^{2+}$, respectively, according to Table S9 (ESI†). The crystal field splitting (ϵ_{cfs} /eV) can be calculated according to the following equation,^{35,36}

$$\epsilon_{\text{cfs}} = \beta_{\text{poly}}^Q R_{\text{av}}^{-2} \quad (1)$$

Both Sr^{2+} and Ba^{2+} are coordinated by nine O atoms, therefore, Eu^{2+} on these two sites should have the same β_{poly}^Q value. Eu^{2+} on the Sr^{2+} site with smaller R_{av} has a higher ϵ_{cfs} value than that on the Ba^{2+} site. The centroid shift (ϵ_c /eV) of 5d levels for Eu^{2+} can be obtained using the following equation,^{35,36}

$$\epsilon_c = 1.79 \times 10^{13} \sum_{i=1}^N \frac{\alpha_{\text{sp}}^i}{(R_i - 0.6\Delta R)^6} \quad (2)$$

Most Ba–O bonds are longer than those of Sr–O according to Table S9 (ESI†). The calculated ϵ_c for Eu^{2+} on Sr^{2+} site is larger than that on Ba^{2+} site. The combination of ϵ_c and ϵ_{cfs} suggests that Eu^{2+} on the Sr^{2+} site should have a smaller energy difference between the lowest 5d level and 4f ground state than Eu^{2+} on the Ba^{2+} site, which corresponds to a longer excitation wavelength of the lowest PLE band for Eu^{2+} on the Sr^{2+} site. Fig. 5a and d show the excitation spectra monitored at 420 and 470 nm, which is in accordance with the calculation results. The Stokes shift is defined as the energy difference between the peak values of PLE and PL bands. Therefore, it is obvious that the Stokes shift of Eu^{2+} on the Ba^{2+} site is much higher than that on the Sr^{2+} site. Therefore, a huge different Stokes shift of Eu^{2+} on Sr^{2+} and Ba^{2+} sites is the main reason for the difference of emission peaks for Eu^{2+} on the two sites. Fig. 6 illustrates the difference for Eu^{2+} ions on Sr^{2+} and Ba^{2+} related sites in the configurational coordinate diagram. For Ba polyhedrons related emission, the excited state of Eu^{2+} suffers a larger offset (ΔR) of the parabola, therefore, resulting in a larger Stokes shift and longer emission wavelength. The PLE bands monitored at 470 and 500 nm for $x = 0.995$ also almost overlap, which is consistent, with that, there is only one Ba site in trigonal

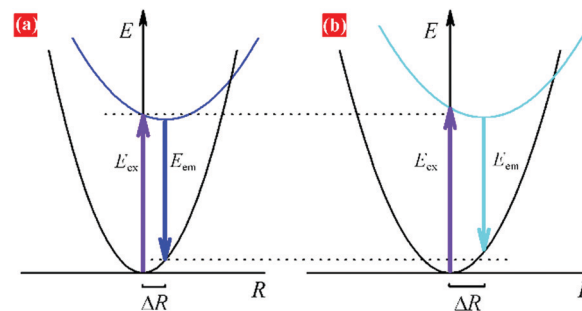


Fig. 6 Configuration coordinate diagram for Eu^{2+} ions on (a) Sr and (b) Ba polyhedrons, illustrating the origin of similar PLE bands but different PL bands.

LiBaPO_4 . The m-, t-, and even h-phase differ in the orientation of LiO_4 and PO_4 , which results in the variation of Sr/ BaO_9 polyhedrons. The change of Ba/Sr ratio is easy to cause the variation of Sr/ BaO_9 polyhedrons. Therefore, the unusual asymmetric PL band at 470 nm may originate from Eu^{2+} ion on Ba^{2+} sites with a slight difference among themselves. Fig. 7 plots the decay curves of samples monitored at 420 and 470 nm. The different decay behaviors for 420 and 470 nm related emissions for $x = 0.3$ again suggest the different coordinate environments. The decay monitored at 420 nm slows down with the increase of Ba^{2+} content from $x = 0$ to 0.3, which suggests that the change of chemical composition and the decrease of Eu^{2+} occupancy on Sr^{2+} -related site lead to the variation in the nonradiative transition rate.

The internal quantum efficiency (QE) of $\text{LiSr}_{0.995-x}\text{Ba}_x\text{PO}_4:0.005\text{Eu}^{2+}$ obtained at 1200 °C was estimated to be about 76.08%, 60.10%, 68.47% and 75.34% for $x = 0, 0.3, 0.9$, and 0.994, respectively. The QE values of the end compounds are higher than those of solid-solution compounds. Related spectra for QE measurements are shown in Fig. S4 (ESI†). The relationship between QE and decay time can be expressed as^{13,37}

$$\text{QE} = \tau/\tau_0 \quad (3)$$

where τ and τ_0 are the decay times with and without nonradiative transition, respectively. The increase of lifetime for 470 nm emission as indicated in Fig. 7b is consistent with the increase of QE value from $x = 0.3$ to 0.995, which suggests the decrease of nonradiative rate.

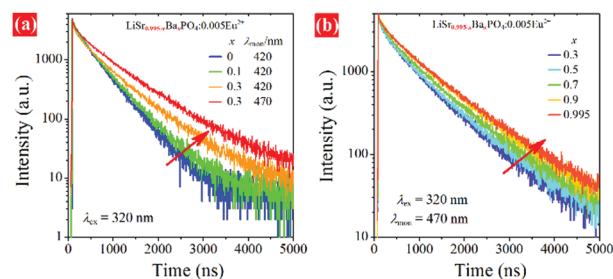


Fig. 7 Decay curves of $\text{LSBPO}:0.005\text{Eu}^{2+}$, (a) monitored at 420 nm for $x = 0 - 0.1$ and at both 420 and 470 nm for $x = 0.3$, (b) monitored at 470 nm for $x = 0.3 - 0.995$.



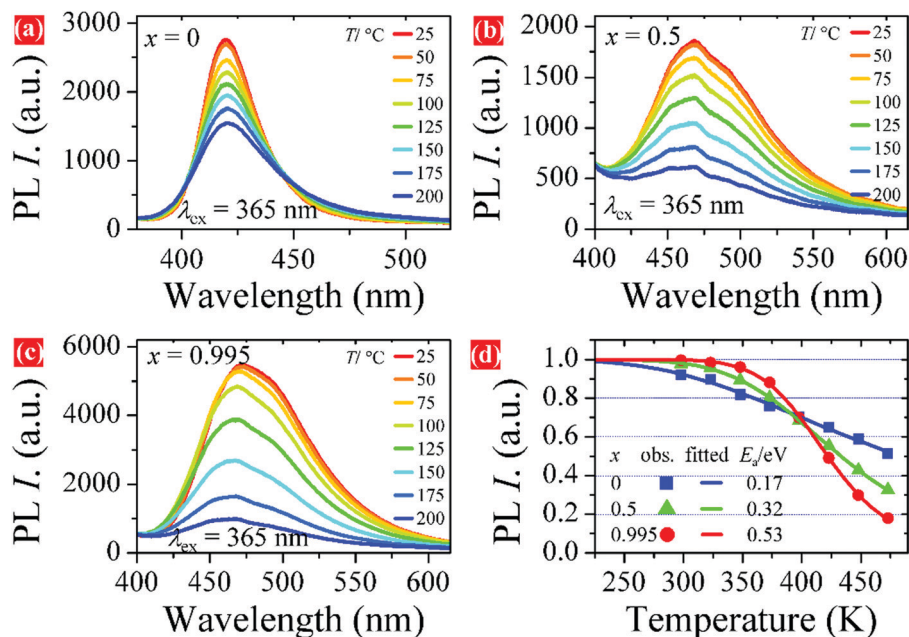


Fig. 8 Temperature-dependent PL spectra of LSBPO:0.005Eu²⁺, (a) $x = 0$, (b) $x = 0.5$, (c) $x = 0.995$, and (d) PL intensity versus temperature with fitted E_a values.

Thermal stability is also an important parameter for phosphors used in pc-LEDs. The temperature-dependent PL spectra of representative samples are shown in Fig. 8a–c. The PL intensity tends to decrease with increasing temperature from room temperature to 200 °C for all samples. Fig. 8d plots the PL intensity versus temperature. It is obvious that the PL intensity of sample $x = 0.995$ drops slowly from 25 to 100 °C and then faster with a further increase in temperature. While the PL

intensity of samples $x = 0$ and 0.5 decreases smoother than that of $x = 0.995$ at higher temperatures. The PL intensity of the samples at 125 °C remains at 75% of the initial value at room temperature. The fitted curves in Fig. 8d are achieved by using the Arrhenius formula,³⁸

$$\frac{I_T}{I_0} = \left[1 + D \exp\left(\frac{-E_a}{kT}\right) \right]^{-1} \quad (4)$$

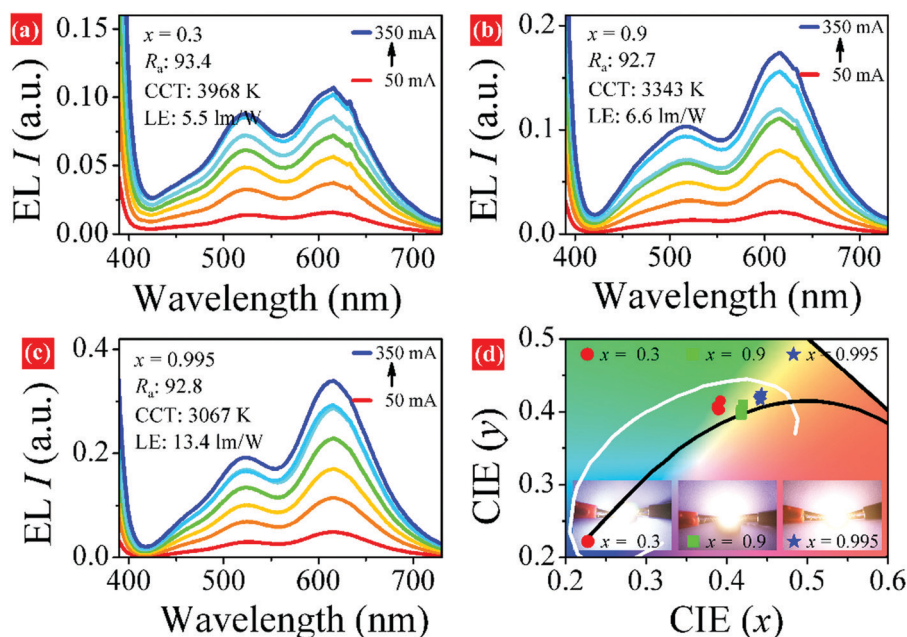


Fig. 9 EL spectra of white pc-LEDs based on LSBPO:0.005Eu²⁺ phosphors combined with 365 nm chip and commercial green and red phosphors, (a) $x = 0.3$, (b) $x = 0.9$, (c) $x = 0.995$, and (d) CIE coordinates of the pc-LEDs under different currents.



where I_T and I_0 are the PL intensity at temperature T (in K) and 0 K, respectively. E_a is the activation energy for thermal quenching. D is a constant depending on phosphor, and k is the Boltzmann constant. The fitted E_a values for $x = 0, 0.5$, and 0.995 are $0.17, 0.32$, and 0.53 eV, respectively. A higher E_a value means that it needs more energy for the excited electrons to return to the ground state nonradiatively. The calculated E_a values are in accordance with the temperature-dependent PL intensity below 125°C . Furthermore, the PL peak of the samples change little upon increasing temperature. The stability of both PL intensity and peak suggests that $\text{LSBPO:0.005Eu}^{2+}$ phosphors could be suitable for pc-LEDs.

A series of white-emitting pc-LEDs were fabricated by combining $\text{LSBPO:0.005Eu}^{2+}$ phosphors and commercial green-emitting $(\text{Ba,Sr})_2\text{SiO}_4\text{:Eu}^{2+}$, red-emitting $\text{CaSiAlN}_3\text{:Eu}^{2+}$ with a 365 nm n-UV chip. The electroluminescent (EL) spectra of the pc-LEDs under $50\text{--}350$ mA forward bias currents are shown in Fig. 9a–c. The performance of the pc-LED based on $\text{LiSrPO}_4\text{:0.005Eu}^{2+}$ ($x = 0$) can be found in our previous work, which contains a gap around the cyan-emission region. However, pc-LEDs based on samples $x = 0.3, 0.9$, and 0.995 can overcome this drawback as these phosphors show emission bands covering the cyan region. All the pc-LEDs have a color-rendering index (R_a) value higher than 90 and a warm white emission with correlated color temperature (CCT) at $3000\text{--}4000$ K. The EL intensities of pc-LEDs tends to increase with working current, and the EL profile changes little. Luminance efficacies (LE) of the pc-LEDs at 50 mA are shown in Fig. 9. It is believed that the LE values can be improved by optimizing the parameters for pc-LED fabrication, for example, the weight ratio of phosphor to silica gel. Fig. 9d shows the CIE coordinates of the pc-LEDs under different current, detailed CIE values *versus* current are plotted in Fig. S5 (ESI[†]). These results suggest that the $\text{LSBPO:0.005Eu}^{2+}$ phosphors can be candidates as blue-emitting component for pc-LEDs based on the n-UV chip.

Conclusions

In summary, emission-tunable Eu^{2+} -activated $\text{LiSr}_{1-x}\text{Ba}_x\text{PO}_4$ solid solution was obtained by a high-temperature solid-state reaction. The crystal structure of a recently refined monoclinic phase can be maintained in $\text{LiSr}_{0.995-x}\text{Ba}_x\text{PO}_4\text{:0.005Eu}^{2+}$ for x in $0\text{--}0.9$ range. While, it crystallizes in a trigonal phase for $\text{LiBa}_{0.995}\text{PO}_4\text{:0.005Eu}^{2+}$ ($x = 0.995$). The end compounds $\text{LiSr}_{0.995}\text{PO}_4\text{:0.005Eu}^{2+}$ and $\text{LiBa}_{0.995}\text{PO}_4\text{:0.005Eu}^{2+}$ exhibit broad emission bands at 420 and 470 nm, respectively. However, no continuous shift of the emission band is observed in the solid solution, although there is only one crystallographic Sr or Ba site in the crystal structure. The formation of nanosegregation is proposed to explain the variation of emission upon changing Ba/Sr ratio in $\text{LiSr}_{0.995-x}\text{Ba}_x\text{PO}_4\text{:0.005Eu}^{2+}$. The work provides an example of controlled photoluminescence tuning with a discontinuous shift of the emission band. Thermal stability and performance of pc-LEDs suggest that the

phosphors can be a candidate as phosphors for solid-state lighting based on n-UV LED.

Conflicts of interest

There are no conflicts of interest to declare.

Acknowledgements

This work is financially supported by Hunan Provincial Natural Science Foundation of China (Grant no. 2019JJ50100), the National Natural Science Foundation of China (Grant no. 21772035, 21505038), and the Scientific Research Fund of Hunan Provincial Education Department (19K024).

Notes and references

- 1 M.-H. Fang, C. O. M. Mariano, P.-Y. Chen, S.-F. Hu and R.-S. Liu, *Chem. Mater.*, 2020, **32**, 1748–1759.
- 2 Y. Wang, J. Ding, Y. Wang, X. Zhou, Y. Cao, B. Ma, J. Li, X. Wang, T. Seto and Z. Zhao, *J. Mater. Chem. C*, 2019, **7**, 1792–1820.
- 3 B. Shao, J. Huo and H. You, *Adv. Opt. Mater.*, 2019, **7**, 1900319.
- 4 J. Qiao, J. Zhao, Q. Liu and Z. Xia, *J. Rare Earths*, 2019, **37**, 565–572.
- 5 M. Zhao, Q. Zhang and Z. Xia, *Acc. Mater. Res.*, 2020, **1**, 137–145.
- 6 G. Li, Y. Tian, Y. Zhao and J. Lin, *Chem. Soc. Rev.*, 2015, **44**, 8688–8713.
- 7 Y. Wei, L. Cao, L. M. Lv, G. G. Li, J. R. Hao, J. S. Gao, C. C. Su, C. C. Lin, H. S. Jang, P. P. Dang and J. Lin, *Chem. Mater.*, 2018, **30**, 2389–2399.
- 8 J. Qiao, L. Ning, M. S. Molokeev, Y.-C. Chuang, Q. Liu and Z. Xia, *J. Am. Chem. Soc.*, 2018, **140**, 9730–9736.
- 9 S. Liao, X. Ji, Y. Liu and J. Zhang, *ACS Appl. Mater. Interfaces*, 2018, **10**, 39064–39073.
- 10 J. Zhong, W. Zhao, F. Du, J. Wen, W. Zhuang, R. Liu, C.-K. Duan, L. Wang and K. Lin, *J. Phys. Chem. C*, 2018, **122**, 7849–7858.
- 11 J. L. Leano, A. Lazarowska, S. Mahlik, M. Grinberg, H. S. Sheu and R. S. Liu, *Chem. Mater.*, 2018, **30**, 4493–4497.
- 12 Y.-C. Lin, P. Erhart, M. Bettinelli, N. C. George, S. F. Parker and M. Karlsson, *Chem. Mater.*, 2018, **30**, 1865–1877.
- 13 X. Ji, J. Zhang, Y. Li, S. Liao, X. Zhang, Z. Yang, Z. Wang, Z. Qiu, W. Zhou, L. Yu and S. Lian, *Chem. Mater.*, 2018, **30**, 5137–5147.
- 14 A. C. Duke, S. Hariyani and J. Brgoch, *Chem. Mater.*, 2018, **30**, 2668–2675.
- 15 L. L. Sun, B. Devakumar, J. Liang, S. Y. Wang, Q. Sun and X. Y. Huang, *J. Mater. Chem. C*, 2020, **8**, 1095–1103.
- 16 M. Zhao, K. Cao, M. Liu, J. Zhang, R. Chen, Q. Zhang and Z. Xia, *Angew. Chem., Int. Ed.*, 2020, **59**, 12938–12943.
- 17 X. X. Sheng, P. P. Dai, Z. Y. Sun and D. W. Wen, *Chem. Eng. J.*, 2020, **395**, 125141.



- 18 J. Zhang, J. Zhang, W. Zhou, X. Ji, W. Ma, Z. Qiu, L. Yu, C. Li, Z. Xia, Z. Wang and S. Lian, *ACS Appl. Mater. Interfaces*, 2017, **9**, 30746–30754.
- 19 Z. Xia, G. Liu, J. Wen, Z. Mei, M. Balasubramanian, M. S. Molokeev, L. Peng, L. Gu, D. J. Miller, Q. Liu and K. R. Poeppelmeier, *J. Am. Chem. Soc.*, 2016, **138**, 1158–1161.
- 20 G. Li, C. C. Lin, W.-T. Chen, M. S. Molokeev, V. V. Atuchin, C.-Y. Chiang, W. Zhou, C.-W. Wang, W.-H. Li and H.-S. Sheu, *Chem. Mater.*, 2014, **26**, 2991–3001.
- 21 Y. Chen, J. Wang, C. Liu, J. Tang, X. Kuang, M. Wu and Q. Su, *Opt. Express*, 2013, **21**, 3161–3169.
- 22 L. Wang, J. Cui, Q. Shi, Y. Tian, C. Cui, M. Ren and P. Huang, *J. Alloys Compd.*, 2018, **764**, 1003–1007.
- 23 C. C. Lin, C.-C. Shen and R.-S. Liu, *Chem. – Eur. J.*, 2013, **19**, 15358–15365.
- 24 S. Liao, Y. Li, Y. Zhang, Z. Tan, X. Fu, Z. Qiu and J. Zhang, *Appl. Mater. Today*, 2020, **21**, 100792.
- 25 S.-C. Kim, J. Kim, H. E. Lee, B. J. Kang, F. Rotermund and S.-J. Kim, *Solid State Sci.*, 2018, **83**, 76–81.
- 26 Z. C. Wu, J. Liu, M. L. Gong and Q. Su, *J. Electrochem. Soc.*, 2009, **156**, H153–H156.
- 27 S. Zhang, Y. Nakai, T. Tsuboi, Y. Huang and H. J. Seo, *Chem. Mater.*, 2011, **23**, 1216–1224.
- 28 J. Sun, X. Zhang, Z. Xia and H. Du, *J. Appl. Phys.*, 2012, **111**, 013101.
- 29 M. W. Wang, W. Lin, N. Liu and Y. P. Ye, *J. Lumin.*, 2018, **194**, 682–685.
- 30 Y. Huang, J. Qin, Z. Fan, D. Wei and H. J. Seo, *Inorg. Chem.*, 2019, **58**, 13161–13169.
- 31 B. H. Toby, EXPGUI, *J. Appl. Crystallogr.*, 2001, **34**, 210–213.
- 32 V. Bachmann, C. Ronda, O. Oeckler, W. Schnick and A. Meijerink, *Chem. Mater.*, 2009, **21**, 316–325.
- 33 S. Xin, M. Gao, C. Wang, X. Wang, G. Zhu, F. Zhou, Z. Li and Y. Wang, *CrystEngComm*, 2018, **20**, 4383–4394.
- 34 W. Wang, M. Tao, Y. Liu, Y. Wei, G. Xing, P. Dang, J. Lin and G. Li, *Chem. Mater.*, 2019, **31**, 9200–9210.
- 35 P. Dorenbos, *J. Lumin.*, 2002, **99**, 283–299.
- 36 P. Dorenbos, *J. Lumin.*, 2003, **105**, 117–119.
- 37 Y. Li, Z. Qiu, J. Zhang, X. Ji, X. Zhang, S. Liao, W. Zhou, L. Yu and S. Lian, *J. Mater. Chem. C*, 2019, **7**, 8982–8991.
- 38 Y.-T. Tsai, C.-Y. Chiang, W. Zhou, J.-F. Lee, H.-S. Sheu and R.-S. Liu, *J. Am. Chem. Soc.*, 2015, **137**, 8936–8939.

